

# DFIR-DETR: Frequency-Domain Iterative Refinement and Dynamic Feature Aggregation for Small Object Detection

Bo Gao<sup>a</sup>, Jingcheng Tong<sup>a</sup>, Xingsheng Chen<sup>b</sup>, Han Yu<sup>c</sup> and Zichen Li<sup>a</sup>

<sup>a</sup>*School of Information Engineering, Beijing Institute of Graphic Communication, Beijing, China*

<sup>b</sup>*School of Computing and Data Science, The University of Hong Kong, Hong Kong SAR, China*

<sup>c</sup>*College of Computing and Data Science, Nanyang Technological University, Singapore*

## ARTICLE INFO

### Keywords:

Small object detection  
Transformer-based detection  
Frequency-domain feature learning  
Sparse attention mechanism  
Multi-scale feature fusion  
Cross-scene generalisation

## ABSTRACT

Small object detection in complex scenes exposes a fundamental tension in neural network design: backbone attention distributes computation uniformly regardless of content, pyramid necks inflate activation magnitudes during upsampling without norm compensation, and bottleneck convolutions progressively smooth high-frequency edge components through accumulated spatial filtering. In response, we develop DFIR-DETR by tracing each proposed module back to a specific, measurable deficiency in the RT-DETR baseline: uniform attention that ignores spatial complexity, norm drift that destabilises upsampled features, and spatial convolutions that progressively suppress the high-frequency components small objects depend on. On NEU-DET and VisDrone, DFIR-DETR achieves 92.9% and 51.6% mAP50 with only 11.7M parameters and 47.2 GFLOPs, demonstrating consistent gains across two qualitatively different detection domains.

## 1. Introduction

Small object detection remains one of the most demanding problems in deep neural network research. Targets occupying fewer than  $32 \times 32$  pixels carry limited texture information, forcing the network to rely heavily on boundary signals and long-range contextual cues that standard architectures are poorly equipped to exploit. The practical stakes differ sharply between the two application domains this work targets. On industrial production lines, a micro-defect missed during hot-rolled steel inspection does not stay missed; mechanical stress concentrates at the undetected boundary and the failure propagates downstream. Throughput constraints are equally unforgiving: frame budgets measured in tens of milliseconds rule out the multi-pass strategies that offline detectors rely on for accuracy. Aerial monitoring from UAVs presents a structurally different version of the same difficulty. At cruising altitude, a pedestrian or cyclist collapses to 10–15 pixels; the surrounding scene is dense and cluttered, so both missed targets and spurious detections carry real operational cost. What unites the two domains is a shared bottleneck: neither can tolerate the loss of high-frequency boundary information that deep spatial filtering progressively introduces. What separates them is everything else: background statistics, object formation mechanism, scale distribution, imaging geometry. A detector that holds up across both is harder to dismiss as a dataset-specific artefact.

The difficulty is further compounded in cross-scene settings, where a single model must generalise across domains as different as UAV aerial imagery and industrial surface inspection.

A closer examination of modern real-time detectors reveals three structural limitations that bear directly on small object performance. First, convolutional backbones allocate attention computation uniformly across the spatial domain, giving equal weight to uninformative backgrounds and

information-dense object boundaries [1]. Second, feature pyramid necks expand activation magnitudes during upsampling without compensating normalisation, disrupting gradient dynamics and degrading cross-scale feature fusion [2]. Third, repeated spatial convolutions act as implicit low-pass filters, attenuating the high-frequency edge components that small objects depend upon for accurate localisation [3].

RT-DETR [4] represents the current state of the art in real-time transformer detection, combining a CNN backbone with a hybrid encoder and an end-to-end query based decoder. However, its ResNet backbone applies fixed-budget attention without content adaptation, its CCFF neck upsamples without amplitude control, and its RepC3 bottleneck operates entirely in the spatial domain, leaving all three limitations unaddressed.

We propose DFIR-DETR, which introduces three architectural contributions corresponding to each identified limitation. The Dynamic Content-Feature Aggregation (DCFA) module parsifies the attention matrix through a dynamic Top-K mechanism predicted from local feature statistics, reducing complexity from  $\mathcal{O}(N^2)$  to  $\mathcal{O}(NK)$ . The Dynamic Feature Pyramid Network (DFPN) introduces norm-preserving upsampling together with a dual-path convolution structure for explicit spatial detail recovery. The Frequency domain Iterative Refinement module (FIRC3) reformulates feature aggregation as a constrained optimisation problem in the spectral domain, where high-frequency boundary components can be explicitly reinforced.

The main contributions of this work are summarised as follows:

- DCFA is introduced as a content-adaptive backbone module, where a dynamic Top-K sparsification mechanism redistributes attention capacity toward structurally complex regions, bringing complexity down

from  $\mathcal{O}(N^2)$  to  $\mathcal{O}(NK)$  without sacrificing global context modelling.

- Drawing on an  $L_1$ -norm conservation argument, DFPN is developed with analytically derived amplitude normalisation during upsampling and a dual-path shuffle convolution for explicit fine-grained spatial detail recovery across pyramid scales.
- The bottleneck feature aggregation problem is reformulated as a frequency-domain least-squares optimisation in FIRC3, granting the network direct and learnable access to high-frequency boundary components that accumulate spatial filtering cannot preserve.
- On NEU-DET and VisDrone, the proposed architecture attains 92.9% and 51.6% mAP50 with only 11.7M parameters and 47.2 GFLOPs, achieving state-of-the-art accuracy while reducing both model size and computational cost relative to the baseline.

The remainder of this paper is organised as follows. Section 2 reviews related work on object detection architectures, attention mechanisms, multi-scale feature fusion, and frequency-domain neural network modules. Section 3 presents the proposed DFIR-DETR framework and details the design of DCFA, DFPN, and FIRC3. Section 4 describes the experimental setup, benchmark datasets, ablation studies, and comparisons with state-of-the-art methods. Section 5 concludes the paper.

## 2. Related Work

### 2.1. Object Detection Architectures

Object detection has undergone two broad paradigm shifts over the past decade. Two-stage methods such as Faster R-CNN [5] separated region proposal from classification, achieving strong accuracy at the cost of inference speed. One-stage detectors including SSD [6] and YOLO [7] collapsed this pipeline into a single forward pass, with YOLOv3 [8] demonstrating that multi-scale prediction heads could recover much of the accuracy lost by removing the proposal stage.

DETR [9] subsequently recast detection as set prediction via bipartite matching, discarding both anchors and non-maximum suppression. Deformable DETR [10], DN-DETR [11], and DINO [12] progressively addressed its convergence and accuracy limitations. RT-DETR brought this line of work to practical deployment by pairing a hybrid encoder with a query-based decoder, achieving real-time throughput while retaining end-to-end training. The present work takes RT-DETR as its starting point, leaving the decoder unchanged while substantially rethinking how features are extracted, fused, and refined prior to decoding.

### 2.2. Attention Mechanisms and Sparse Computation

Attention has become the central computational primitive in modern vision networks, yet its quadratic cost with respect to sequence length remains a persistent bottleneck. Local window attention [13] confines each token to a bounded spatial neighbourhood, improving throughput but weakening the long-range dependency modelling critical for small object detection. Deformable attention [10] maintains linear cost by sampling a fixed number of reference points per query, but loses the ability to adapt to local feature complexity. Token merging approaches [14] combine redundant tokens to reduce sequence length, yet the resulting loss of positional specificity is detrimental for localisation-sensitive tasks. In detection, sparse query designs appear in Sparse DETR [15] and Efficient DETR [16], which reduce computational load by selecting informative encoder tokens. However, these methods fix the sparsification threshold globally, whereas the informational density of a feature map varies substantially between defect-heavy industrial images and sparsely populated aerial frames. DCFA addresses this by predicting the retention ratio from local feature statistics, making sparsification content-dependent rather than scene-agnostic, and pairs the resulting sparse attention with a spatial gated linear unit that enriches nonlinear channel transformations with neighbourhood context.

### 2.3. Multi-Scale Feature Fusion

Feature pyramids [17] established the principle of combining semantic richness from deep layers with spatial precision from shallow layers through a top-down pathway with lateral connections. PANet [18] augmented this with a complementary bottom-up path, shortening the information routing distance between low-level detail and high-level semantics. BiFPN, introduced within EfficientDet [19], went further by learning scalar weights for each cross-scale connection, allowing the network to modulate the relative contribution of each resolution level during fusion. Despite these refinements, a complication common to all pyramid designs has received little attention: upsampling expands feature map area by  $s^2$ , inflating the  $L_1$  norm of activations and disrupting gradient balance between upsampled and lateral paths. SlimNeck [20] and Gold-YOLO [21] improve feature routing efficiency but leave this amplitude drift uncorrected. DFPN compensates through an analytically derived normalisation factor, providing stable cross-scale fusion that prior designs do not offer.

### 2.4. Frequency-Domain Representations in Neural Networks

The motivation for incorporating spectral operations into detection networks has both efficiency and representational grounds. Phase-aware MLP architectures [22] demonstrated that decomposing image patches into amplitude and phase components enables richer spatial modelling than purely spatial mixing, establishing that frequency-domain parameterisation captures structure that spatial convolutions miss.

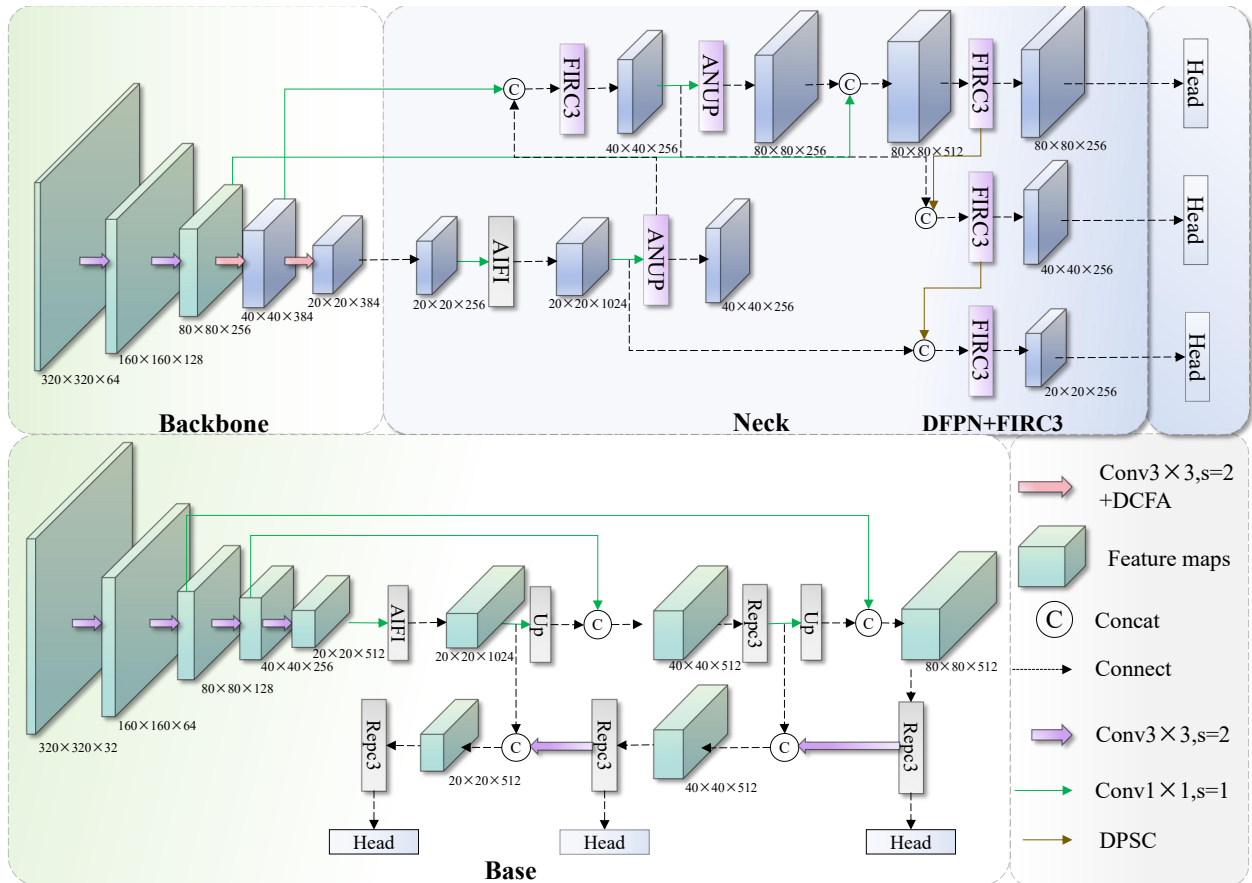


Figure 1: Overall architecture of DFIR-DETR.

Beyond representational benefits, the computational argument is compelling: a convolution of kernel size  $k$  over a spatial map of size  $N$  costs  $\mathcal{O}(Nk^2)$ , whereas the equivalent spectral operation requires only  $\mathcal{O}(N \log N)$  regardless of effective receptive field size.

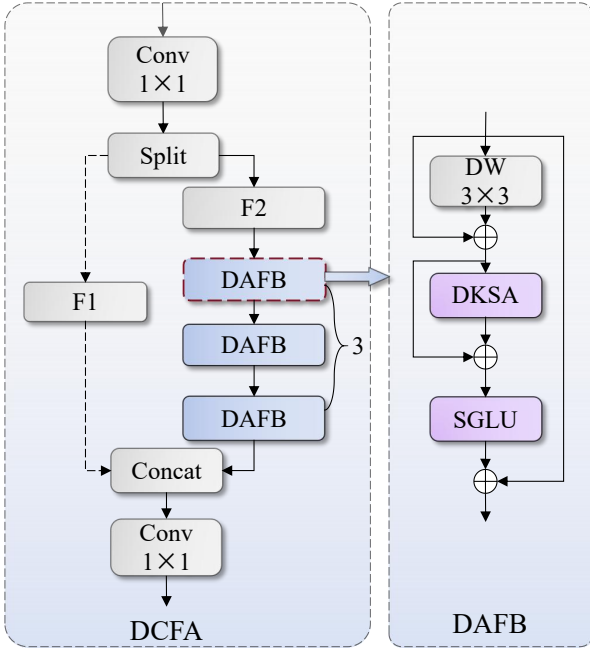
Among classification-oriented frequency methods, FcaNet [23] decomposes channel attention into discrete cosine components, GFNet [24] substitutes spatial token-mixing layers with global Fourier filters, and FocalNet [25] aggregates context at multiple scales through focal modulation. These methods enrich feature representations within a single resolution stage but do not engage with the cross-scale fusion problem. Within the detection literature, SF-DETR [26] injects scale-frequency awareness into the encoder to capture high-frequency boundary cues in drone-view scenes, and Freq-DETR [27] constructs dual-branch processing to jointly model spatial and frequency features for UAV imagery. Both methods treat frequency as a supplementary signal alongside spatial features, however, rather than as the exclusive medium for bottleneck computation. FIRC3 departs from this pattern by fully relocating feature refinement into the spectral domain and solving the resulting problem as a constrained least-squares optimisation, giving the network direct and learnable control over the high-frequency content that governs boundary localisation for small objects.

### 3. Methods

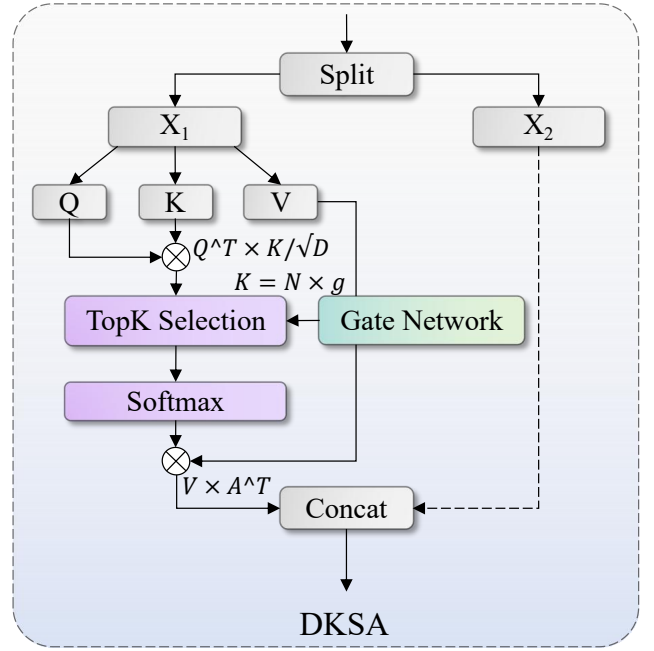
We propose DFIR-DETR to address small object detection challenges in UAV remote sensing and industrial surface inspection. The architecture, illustrated in Fig. 1, tackles two fundamental problems: sparse feature representation of distant small objects in VisDrone and subtle defect texture capture in NEU-DET. DCFA serves as the Backbone, where content-adaptive K-sparse attention allocates computational resources dynamically—defect regions and small targets receive concentrated modeling while uniform backgrounds undergo aggressive pruning. DFPN functions as the Neck, preventing feature inflation during upsampling through amplitude normalization and retaining fine spatial details through dual-path shuffle convolution across scales. FIRC3 operates in the feature fusion layer, processing features in the frequency domain to capture global context at reduced computational cost. Each component targets specific failure modes of existing detectors: DCFA addresses limited receptive fields, DFPN prevents information loss during scale transitions, and FIRC3 preserves high-frequency boundary details.

#### 3.1. DCFA

The backbone of conventional RT-DETR relies on a ResNet architecture composed of homogeneous BasicBlock



(a) DCFA block



(b) DKSA block

modules stacked uniformly across all stages. However, this design exhibits three limitations that become particularly pronounced in cross-scene small object detection. Progressive downsampling erodes the fine-grained geometric detail and edge continuity that small objects and subtle surface defects depend upon, while the fixed receptive field expansion schedule lacks the flexibility to accommodate the wide scale range encountered across different scenes. Furthermore, without explicit spatial attention, the network cannot suppress irrelevant background activations in dense or cluttered environments, leaving both false positive and false negative rates persistently high. To address these limitations, we propose DCFA, a content-adaptive feature aggregation backbone that treats representational allocation as a learnable function of local feature complexity. The key innovation is learning to allocate computational resources based on local complexity: small object regions receive concentrated attention modeling through dynamic K-sparse selection (DKSA), while uniform backgrounds are efficiently pruned. Spatial gated linear units (SGLU) further incorporate neighborhood context into nonlinear transformations. This design simultaneously preserves fine-grained geometric details and high-level semantic information, as illustrated in Fig. 2a.

The DCFA module adopts a cross-stage partial (CSP) network architecture, achieving gradient-efficient propagation and multi-scale feature fusion through dual-path feature flows. The complete feature transformation process can be mathematically formulated as:

$$Y = \phi_{cv2} \left( \text{Concat} [F_1, F_2, G_1(F_2), G_2(G_1(F_2)), \dots, G_n(G_{n-1}(\dots))] \right), \quad (1)$$

$$[F_1, F_2] = \text{split}(\phi_{cv1}(X)) \quad (2)$$

where  $G_i$  represents the  $i$ -th DAFB (Dynamic Attention Fusion Block) transformation operator,  $n$  denotes the stacking depth, and  $\phi_{cv1}$  and  $\phi_{cv2}$  represent the input and output  $1 \times 1$  convolutional projection layers, respectively.

DAFB achieves comprehensive feature enhancement by cascading three functionally complementary sub-modules. Its forward propagation follows the transformation chain:

$$\begin{aligned} Z &= \text{SGLU}(H + \text{DKSA}(H)), \\ H &= X + \phi_{dw}(X) \end{aligned} \quad (3)$$

where  $\phi_{dw}$  denotes a  $3 \times 3$  depthwise separable convolution with batch normalization. The DKSA mechanism subsequently operates on the enhanced features  $H$ , selectively focusing on defect regions in industrial scenarios through dynamic sparsification strategies while establishing long-range associations between small objects and contexts in remote sensing scenarios. SGLU serves as a feedforward network to perform nonlinear transformation and channel mixing on attention-enhanced features. Its gating mechanism adaptively modulates the activation intensity of different channels, further improving cross-scene feature discriminability. The mathematical expression is:

$$\text{SGLU}(X) = X + \phi_{out} \left( \mathcal{D} \left( \left( \phi_{act} \left( \phi_{dw}^{3 \times 3} (X_g) \right) \right) \odot X_v \right) \right) \quad (4)$$

$\phi_{dw}^{3 \times 3}$  represents the  $3 \times 3$  depthwise convolution applied to the gating stream, encoding local spatial contextual information into gating signals so that gating decisions integrate

neighborhood spatial patterns rather than relying solely on single-point feature values.  $\phi_{act}$  employs the GELU activation function, providing smoother gradient flow compared to ReLU. Element-wise multiplication  $\odot$  implements gating modulation, and  $\mathcal{D}$  denotes Dropout regularization.

DKSA implements computationally efficient self-attention through a dynamic Top-K selection strategy, demonstrating excellent adaptability in both industrial defect detection and remote sensing small object recognition scenarios, as illustrated in Fig. 2b. Combined with LGN (Layer Group Normalization) preprocessing, the complete attention computation process can be uniformly expressed as:

$$\text{DKSA}(X) = \phi_{proj} \left( \text{Concat} \left[ (VA^T)^{reshape}, X_2 \right] \right) \quad (5)$$

$$A_{ij} = \begin{cases} \frac{\exp(s_{ij})}{\sum_{j' \in \mathcal{T}_K^i} \exp(s_{ij'})}, & j \in \mathcal{T}_K^i \\ 0, & j \notin \mathcal{T}_K^i \end{cases} \quad (6)$$

The dynamic Top-K selection mechanism is defined as:

$$K = \lfloor N \cdot \sigma(\text{AvgPool}(\psi(X))) \rfloor \quad (7)$$

where  $\psi$  represents a gating network composed of two convolutional layers,  $\sigma$  denotes the sigmoid function, and the output scalar value determines the proportion of attention connections to retain.  $\mathcal{T}_K^i = \text{TopK}(S_i, K)$  returns the index set of the top  $K$  most relevant key positions for the  $i$ -th query position. Unselected connections are masked to zero, thereby converting the attention matrix from dense to structurally sparse, reducing computational complexity from  $\mathcal{O}(N^2)$  to  $\mathcal{O}(NK)$ .

---

#### Algorithm 1 DCFA

---

**Require:** Input feature map  $X \in \mathbb{R}^{C \times H \times W}$ , stack depth  $N$

**Ensure:** Enhanced feature map  $Y \in \mathbb{R}^{C \times H \times W}$

```

1:  $X_1, X_2 \leftarrow \text{Split}(X)$  // Dual-path feature flow
2:  $F \leftarrow X_1$ 
3: for  $i = 1$  to  $N$  do
4:   // Dynamic Attention Fusion Block
5:    $F' \leftarrow \text{DWConv}_{3 \times 3}(F) + \text{BN}(F)$ 
6:   // Dynamic K-Sparse Attention
7:    $F'' \leftarrow \text{LGN}(F')$ 
8:    $Q, K, V \leftarrow \text{Linear}(F'')$ 
9:    $\rho \leftarrow \sigma(\text{Gate}(F''))$ 
10:   $k \leftarrow \lfloor \rho \cdot HW \rfloor$ 
11:  for each position  $j$  in  $[1, HW]$  do
12:     $T_k^j \leftarrow \text{TopK}(Q_j \cdot K^T, k)$ 
13:     $\text{Attn}_j \leftarrow \text{Softmax} \left( \frac{Q_j \cdot K^T}{\sqrt{d}} \right) \cdot V_{T_k^j}$ 
14:  end for
15:  // Spatial Gated Linear Unit
16:   $G \leftarrow \text{GELU}(\text{DWConv}_{3 \times 3}(\text{Attn}))$ 
17:   $F \leftarrow \text{Dropout}(\text{Linear}(\text{Attn}) \odot G)$ 
18: end for
19:  $Y \leftarrow \text{Conv}_{1 \times 1}(\text{Concat}(F, X_2))$ 
20: return  $Y$ 

```

---

The dynamic K-sparse attention pruning mechanism enables content-adaptive allocation of computational resources, focusing more attention connections on defect regions in industrial scenarios to capture subtle textures while performing aggressive pruning on uniform backgrounds to reduce redundancy. In remote sensing scenarios, it allocates sufficient contextual modeling capability to small objects while sparsifying large irrelevant backgrounds, achieving optimal trade-offs between accuracy and efficiency in both scenarios. The spatial gated linear unit provides nonlinear modeling capability far exceeding traditional ReLU through spatialized gating signals. Its smooth gradient characteristics avoid gradient vanishing problems, enabling stable training of deep networks and learning of more refined feature transformations. The learnable gating mechanism in Eq. (7) adaptively determines  $K$  based on local feature statistics, which can be interpreted as adaptively balancing representational capacity against computational budget. This enables the network to automatically adjust the trade-off between efficiency and accuracy for each input sample based on scene complexity.

### 3.2. DFPN

The cross-scale feature fusion module CCFF in conventional RT-DETR relies on simple nearest neighbor upsampling and direct concatenation operations for multi-scale feature integration. However, abrupt transitions between feature scales introduce semantic discontinuities, compromising feature representation quality with particularly significant impact on small objects where spatial resolution is critical. The symmetric top-down pathway lacks sufficient consideration of information density differences between scales, resulting in suboptimal feature fusion performance in small object detection tasks. To address these fundamental deficiencies of CCFF, we propose DFPN, a principled redesign of multi-scale feature fusion guided by two core insights: upsampling must preserve feature intensity to prevent gradient instability, and downsampling must retain spatial details critical for small object boundaries. We achieve this through amplitude-normalized upsampling (ANUP) in the top-down pathway that maintains consistent feature magnitudes across scales, and dual-path shuffle convolution (DPSC) in the bottom-up pathway that explicitly preserves fine-grained spatial information during aggregation.

DFPN addresses feature inflation through amplitude-normalised upsampling in the top-down pathway and recovers spatial detail via dual-path shuffle convolution in the bottom-up pathway, as illustrated in Fig. 3 and Fig. 4.

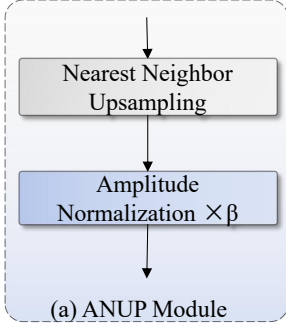


Figure 3: ANUP module.

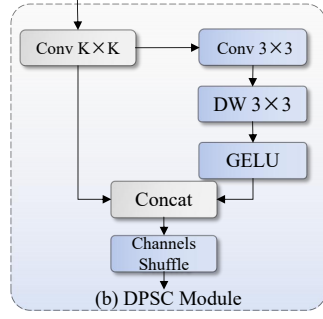


Figure 4: DPSC module.

In the top-down pathway, the ANUP module reconstructs traditional upsampling operations by introducing amplitude-dependent normalization factors to compensate for feature amplitude inflation caused by spatial expansion. Given an input feature map  $F_i$  at scale  $i$ , the ANUP operation produces amplitude-controlled upsampled feature maps:

$$F_i^\uparrow = \beta \cdot \mathcal{U}(F_i) = \frac{1}{s^2} \cdot \mathcal{U}(F_i) \quad (8)$$

where  $\mathcal{U}(\cdot)$  denotes the nearest neighbor upsampling operator with scale factor  $s$ , and  $\beta = 1/s^2$  represents the amplitude normalization coefficient, maintaining consistent feature intensity across different scales. This normalization strategy ensures that upsampled features retain original information density, preventing the feature map inflation common in traditional CCFU upsampling operations. The theoretical foundation stems from the fact that spatial interpolation inherently amplifies the feature map  $L_1$  norm by a factor proportional to the square of the upsampling ratio. The proposed amplitude normalization counteracts this effect by maintaining the relationship:

$$\begin{aligned} \|F_i^\uparrow\|_1 &\approx \|F_i\|_1 \cdot \frac{s^2 \cdot H \cdot W}{H \cdot W} \cdot \frac{1}{s^2} \\ &= \|F_i\|_1 \end{aligned} \quad (9)$$

establishing a more stable feature propagation mechanism, which is particularly significant for preserving subtle appearance features of small objects.

In the bottom-up pathway, the DPSC module addresses information loss during downsampling through a dual-path architecture. The first path performs standard convolution to extract semantic features, while the second path takes the output of the first path as input, capturing spatial details through cascaded convolutions, ultimately fusing dual-path information through channel shuffling. The DPSC operation is formulated as:

$$F_{out} = \mathcal{M}\left(\text{Concat}\left(F_1^{std}, \phi\left(W_d * (W_{conv} * F_1^{std})\right)\right)\right) \quad (10)$$

## Algorithm 2 DFPN

**Require:** Multi-scale features  $\{F_i\}_{i=1}^L$ , scale  $s$

**Ensure:** Enhanced features  $\{F_i^{out}\}_{i=1}^L$

```

1:  $F_L^{up} \leftarrow F_L$ 
2: // Top-down with ANUP
3: for  $i = L - 1$  down to 1 do
4:    $F_i^{up} \leftarrow \text{ANUP}(F_{i+1}^{up}, F_i, s)$ 
5: end for
6: // Apply DPSC
7: for  $i = 1$  to  $L$  do
8:    $F_i^{out} \leftarrow \text{DPSC}(F_i^{up})$ 
9: end for

10: Procedure ANUP( $F_{high}, F_{low}, s$ ):
11:    $F_{up} \leftarrow \text{Upsample}(F_{high}, s)$ 
12:    $F_{norm} \leftarrow (1/s^2) \cdot F_{up}$  // Amplitude normalization
13:   return Conv $_{1 \times 1}$ (Concat( $F_{norm}, F_{low}$ ))

14: Procedure DPSC( $F$ ):
15:    $F_1 \leftarrow \sigma(W_{std} * F)$  // Path 1
16:    $F_2 \leftarrow \text{GELU}(W_d * \text{GELU}(W_{pw} * F))$  // Path 2
17:   return ChannelShuffle(Concat( $F_1, F_2$ ))

```

$F_1^{std}$  represents semantic features extracted through standard convolution with activation function  $\sigma(\cdot)$ ,  $W_{conv}$  and  $W_d$  denote the  $3 \times 3$  standard convolution kernel and  $3 \times 3$  depthwise convolution kernel (groups=C/2) in the second path respectively,  $\phi(\cdot)$  represents the GELU activation function providing smooth gradient flow, and  $\mathcal{M}(\cdot)$  denotes the channel shuffle operation. The channel shuffle mechanism is mathematically represented as a tensor rearrangement operation:

$$\mathcal{M}(F) = \text{Reshape}\left(\text{Permute}\left(\text{Reshape}(F, [B, 2, C/2, H, W]), [0, 2, 1, 3, 4], [B, C, H, W]\right)\right) \quad (11)$$

reorganizing feature channels to facilitate cross-path information exchange. The second path in DPSC constitutes a spatial detail capture branch, taking the output  $F_1^{std}$  of the first path as input and achieving fine-grained feature extraction through cascaded convolution operations:

$$F_2^{dep} = \phi\left(W_d * (W_{conv} * F_1^{std})\right) \quad (12)$$

where  $W_{conv}$  is a  $3 \times 3$  standard convolution kernel for initial spatial feature transformation, and  $W_d$  is a  $3 \times 3$  depthwise convolution kernel for efficient spatial filtering. Through grouped operations, spatial features are progressively refined while maintaining computational efficiency, with GELU activation ensuring smooth gradient propagation required for training stability. The concatenation and shuffling of features from both paths establish comprehensive feature representations, integrating semantic information from the standard convolution path with fine-grained spatial details from the cascaded convolution path.

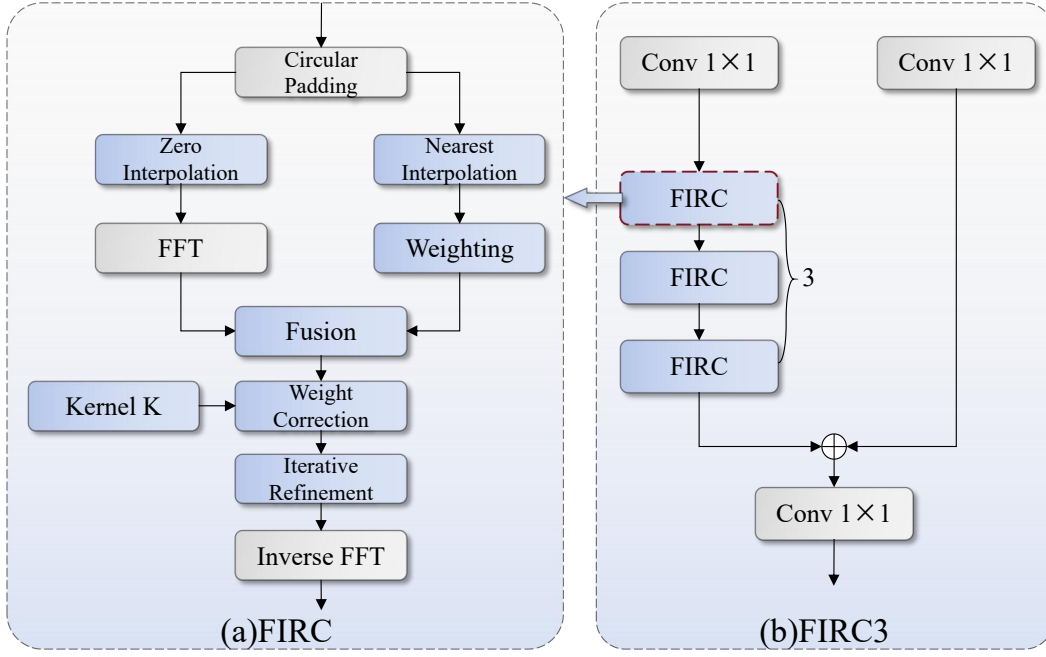


Figure 5: FIRC3 block

ANUP stabilises top-down propagation by eliminating the norm inflation inherent in standard upsampling, ensuring high-level semantic information reaches lower scales with preserved intensity, a property particularly valuable for small objects that depend heavily on contextual cues. DPSC complements this by routing fine-grained boundary detail through a dedicated cascaded convolution stream, so spatial precision is not sacrificed during bottom-up aggregation. The result is more consistent cross-scale feature flow and improved localisation accuracy for small objects across both industrial and aerial detection scenarios.

### 3.3. FIRC3

Conventional RT-DETR employs the RepC3 module for multi-scale feature fusion in its feature pyramid network and path aggregation network structures. However, RepC3 primarily relies on spatial domain convolution operations, exhibiting inherent limitations in capturing long-range dependencies and processing small object features. The spatial locality constraint of conventional convolutions limits the receptive field scope, resulting in insufficient feature representation capability for small objects, while contextual information is crucial for small object detection. Repeated application of spatial domain convolutions introduces cumulative information loss, particularly severely affecting fine-grained details that small object detection depends upon. Targeting these limitations, we propose a novel feature aggregation module FIRC3, which leverages frequency domain transformations to enhance feature propagation and maintain the integrity of small object information throughout the detection pipeline, as illustrated in Fig. 5.

The input feature map  $X$  first generates intermediate representations through two parallel  $1 \times 1$  convolutions. One

branch undergoes cascaded FIRC (Frequency Iterative Refinement Convolution) transformation processing, while the other branch maintains the original feature flow. The module output is formulated as:

$$Y = W_3 (\mathcal{M}(W_1 * X) + W_2 * X) \quad (13)$$

where  $W_1, W_2$  represent channel projection operators,  $\mathcal{M}(\cdot)$  denotes the transformation sequence composed of  $n$  cascaded FIRC operations,  $W_3$  performs final channel mapping,  $*$  denotes convolution operation, and the hidden channel dimension  $C' = \lfloor e \cdot C_{\text{out}} \rfloor$  is controlled by expansion ratio  $e$ . The FIRC operator executes feature transformations in the frequency domain through a convex optimization framework. For a given feature map  $F$ , the FIRC operation first applies circular padding to enable seamless frequency domain processing, subsequently generating sparse and dense upsampled features through zero-interpolation upsampling  $\mathcal{U}_s(F)$  and nearest-neighbor interpolation  $\mathcal{I}_s(F)$  respectively. Define the frequency domain intermediate variable:

$$F_R = \mathcal{F}[K]^* \odot \mathcal{F}[\mathcal{U}_s(F)] + \mathcal{F}[\epsilon_b \cdot \mathcal{I}_s(F)] \quad (14)$$

where  $\mathcal{F}[\cdot]$  denotes the Fast Fourier Transform,  $K$  represents the depthwise separable frequency domain convolution kernel initialized through softmax normalization,  $(\cdot)^*$  denotes complex conjugate operation,  $\odot$  represents element-wise product,  $\epsilon_b = \sigma(b - 9.0) + \epsilon$  is the adaptive regularization term,  $\sigma(\cdot)$  is the sigmoid function, and  $\epsilon = 10^{-5}$  ensures numerical stability. This formula decomposes the

original features into two pathways: the zero-interpolation path preserves precise information at original sampling positions, while the dense interpolation path provides smooth spatial continuity. Through the conjugate of the frequency domain convolution kernel and linear combination of both paths, adaptive fusion of multi-scale features is achieved. Based on  $F_R$ , the adaptive weight correction factor is computed:

$$W_{\text{inv}} = \frac{\text{Avg}_s(\mathcal{F}[K] \odot F_R)}{\text{Avg}_s(|\mathcal{F}[K]|^2) + \epsilon_b} \quad (15)$$

The averaging operator  $\text{Avg}_s(\cdot)$  performs spatial downsampling on frequency domain responses, implementing frequency-selective aggregation by rearranging the spectrum into  $s \times s$  blocks and averaging along the last dimension. The numerator term  $\mathcal{F}[K] \odot F_R$  computes the response intensity between the frequency domain convolution kernel and intermediate features, while the denominator term  $|\mathcal{F}[K]|^2$  represents the squared magnitude of the frequency domain energy spectrum, serving a normalization role to prevent excessive amplification of frequency domain responses. The final output is obtained through frequency domain iterative solving:

$$\hat{F}_{\text{out}} = \mathcal{F}^{-1} \left[ \frac{F_R - \mathcal{F}[K]^* \odot \text{Repeat}_s(W_{\text{inv}})}{\epsilon_b} \right] \quad (16)$$

where  $\mathcal{F}^{-1}[\cdot]$  denotes the inverse Fourier transform, and  $\text{Repeat}_s(\cdot)$  upsamples the downsampled weight factor to the original frequency domain resolution. The subtracted term  $\mathcal{F}[K]^* \odot \text{Repeat}_s(W_{\text{inv}})$  in the numerator can be understood as refined correction of coarse-scale responses, implementing backpropagation through frequency domain conjugate operations, thereby suppressing low-frequency redundancy while maintaining high-frequency details. The entire transformation process essentially solves a frequency-domain-constrained least squares problem, adaptively balancing contributions of different frequency components and enabling the network to dynamically adjust sensitivity to high-frequency information of small objects. Periodization processing of the frequency domain convolution kernel is achieved through point spread function to optical transfer function conversion:

$$\mathcal{F}[K_{\text{circ}}] = \mathcal{F} \left[ \text{Roll}(\text{ZeroPad}(K, (H_s, W_s)), (-\lfloor k/2 \rfloor, -\lfloor k/2 \rfloor)) \right] \quad (17)$$

where  $\text{ZeroPad}(\cdot)$  pads the convolution kernel to the target feature map size, and  $\text{Roll}(\cdot)$  performs circular shift to align the kernel center to the coordinate origin, thereby achieving true circular convolution. Frequency domain operations possess the natural advantage of global receptive fields compared to spatial domain convolutions, enabling the network

---

### Algorithm 3 FIRC3

---

**Require:** Input feature  $X \in \mathbb{R}^{C \times H \times W}$ , iterations  $T$

**Ensure:** Refined feature  $Y \in \mathbb{R}^{C \times H \times W}$

```

1:  $X_1, X_2 \leftarrow \text{Split}(X)$  // Dual-path split
2:  $F \leftarrow X_1$ 
3: for  $t = 1$  to  $T$  do
4:   // Frequency-domain transformation
5:    $F_{\text{freq}} \leftarrow \text{FFT}(F)$ 
6:    $F_{\text{amp}} \leftarrow |F_{\text{freq}}|$  // Amplitude
7:    $F_{\text{phase}} \leftarrow \angle F_{\text{freq}}$  // Phase
8:   // Frequency-domain feature processing
9:    $F'_{\text{amp}} \leftarrow \text{Conv}_{1 \times 1}(F_{\text{amp}})$ 
10:   $F'_{\text{phase}} \leftarrow \text{Conv}_{1 \times 1}(F_{\text{phase}})$ 
11:  // Reconstruct and inverse transform
12:   $F'_{\text{freq}} \leftarrow F'_{\text{amp}} \cdot e^{i \cdot F'_{\text{phase}}}$ 
13:   $F' \leftarrow \text{IFFT}(F'_{\text{freq}})$ 
14:  // Residual connection
15:   $F \leftarrow F + \text{GELU}(\text{Conv}_{3 \times 3}(F'))$ 
16: end for
17:  $Y \leftarrow \text{Conv}_{1 \times 1}(\text{Concat}(F, X_2))$ 
18: return  $Y$ 

```

---

to capture long-distance feature dependencies without increasing parameter count. Through learnable frequency domain convolution kernel parameterization, the module can dynamically adjust sensitivity to different frequency components, better adapting to feature distribution characteristics of objects at different scales.

Operating in the spectral domain grants FIRC3 an implicit global receptive field at  $\mathcal{O}(N \log N)$  cost, while the iterative correction mechanism suppresses low-frequency redundancy and restores the boundary-defining high-frequency signal that repeated spatial convolutions progressively attenuate. The result is more precise localisation of small objects whose appearance is predominantly encoded in fine-scale edge structure.

## 4. Experiments

### 4.1. Experimental Setup

All experiments were conducted on an NVIDIA GeForce RTX 3090 GPU. DFIR-DETR was implemented in PyTorch 2.2.2 / TorchVision 0.17.2, configured based on RT-DETR-R18. Training used AdamW with learning rate  $1 \times 10^{-4}$  and weight decay  $5 \times 10^{-4}$ , for 300 epochs with batch size 4, input resolution  $640 \times 640$ , and mixed-precision training. Average GPU memory consumption was 11 GB and training required 7 hours per dataset.

### 4.2. Benchmark Datasets

These two benchmarks were not chosen arbitrarily. Prior work on small object detection tends to evaluate on a single domain, leaving open the question of whether reported gains reflect architectural improvements or dataset-specific overfitting. VisDrone and NEU-DET differ in sensor type, scene structure, object formation mechanism, and background statistics, but they both expose the same underlying bottleneck:

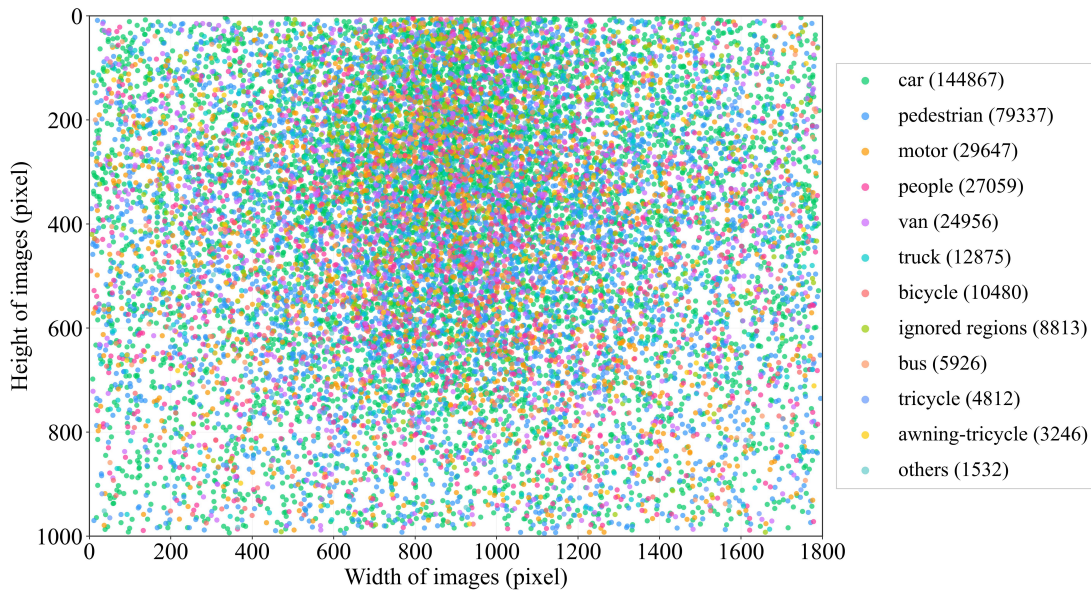


Figure 6: VisDrone object instance spatial distribution.

insufficient high-frequency boundary representation for objects with limited pixel support. Demonstrating consistent gains across both settings provides stronger evidence that the proposed modules address a general architectural deficiency rather than a narrow application-specific one.

**VisDrone** [28] contains 10,209 aerial images with 2.6M bounding boxes across 10 categories. The dataset splits into 6,471 training, 548 validation, and 3,190 testing images, presenting challenges of large scale variations, dense occlusions, and viewpoint diversity, as illustrated in Fig. 6.

**NEU-DET** [29] comprises 1,800 grayscale images of hot-rolled steel surfaces with six defect types (crazing, inclusion, patches, pitted surface, rolled-in scale, scratches), each with 300 images at  $200 \times 200$  pixels. Challenges include subtle texture variations, complex backgrounds, and high inter-class similarity, as illustrated in Fig. 7.

### 4.3. Ablation Study

Table 1 reports ablation results on NEU-DET under two complementary protocols: sequential module addition and single-module removal from the complete model. DCFA alone lifts mAP50 by 1.4 points over the RT-DETR baseline while trimming parameters from 19.9M to 13.7M; the 31.2% reduction comes from the sparse attention structure, not from any sacrifice in representational depth. Substituting only DFPN into the baseline reaches 90.9% mAP50, with the Ri category gaining 11.2 points over baseline, the largest single-category swing in the table; this is consistent with ANUP counteracting the norm inflation that standard upsampling introduces at that scale. FIRC3 alone reaches 90.5% mAP50 at the lowest GFLOPs of any single-module configuration, reflecting the computational advantage of spectral operations over repeated spatial convolutions. The complete model reaches 92.9% mAP50 and 65.9% mAP50:95; the 7.7-point mAP50:95 margin over baseline outpaces the mAP50 margin, which points

to boundary localisation rather than coarse classification as the primary beneficiary. Parameter count and GFLOPs land at 11.7M and 47.2, down 41.2% and 17.2% from the starting point.

Removal experiments invert the construction protocol. Taking DCFA out of the full model costs 1.8 mAP50 points; removing DFPN costs 1.2 points; removing FIRC3 costs 0.5 points. The ordering matches the sequential results: DCFA contributes most on NEU-DET, where content-adaptive sparsification has the sharpest effect on defect boundary discrimination, and confirms that the gains are not an artefact of module interaction alone.

### 4.4. Comparative Performance Analysis and Qualitative Visualisation

On NEU-DET, DFIR-DETR reaches 92.9% mAP50, surpassing the RT-DETR baseline by 4.2 points and YOLOv11m by 0.3 points while reducing parameters to 11.7M, a 77.2% reduction relative to YOLOv6m at substantially higher accuracy, as shown in Table 4. The mAP50:95 gap over baseline is 7.7 points, larger than the mAP50 gap, indicating that frequency-domain boundary recovery contributes more to tight localisation than to coarse detection. Beyond general-purpose detectors, Table 4 also incorporates three methods developed specifically for steel surface inspection: IMN-YOLOv3 [30], FC-DETR [31], and MDT-Net [32]. Despite their domain-specific design, the best-performing specialist method, IMN-YOLOv3, achieves 86.9% mAP50, leaving a gap of at least 6.0 points relative to DFIR-DETR’s 92.9%. Concurrently, FC-DETR requires 56.5M parameters to achieve 83.7%, nearly five times the footprint of our model at comparable or lower accuracy. The pattern suggests that frequency-domain boundary modelling addresses a representational gap that domain-specific architectural choices alone have not closed.

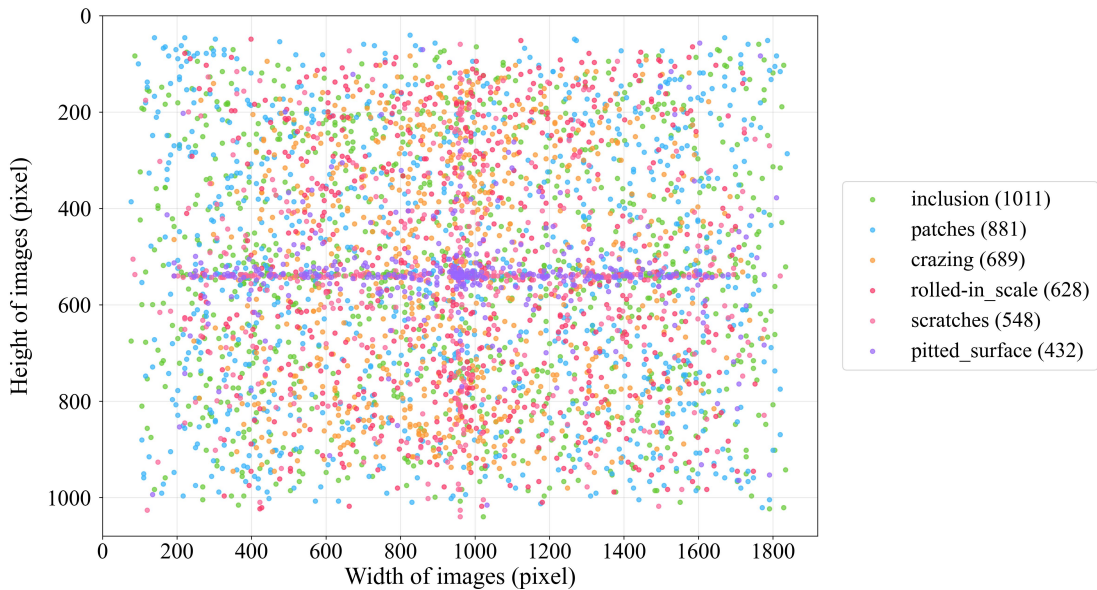


Figure 7: NEU-DET defect instance spatial distribution.

Table 1

Ablation study on NEU-DET dataset.													
DCFA	DFPN	FIRC3	mAP50	Cr	In	Pa	Ps	Ri	Sr	mAP50:95	Params	GFLOPs	FPS
×	×	×	88.7	78.4	87.0	96.0	94.6	78.0	98.1	58.2	19.9	57.0	36.9
✓	×	×	90.1	78.9	91.2	<b>97.0</b>	96.8	84.0	98.6	60.8	13.7	51.7	37.0
×	✓	×	90.9	72.1	94.5	97.0	94.4	89.2	98.3	62.6	19.7	56.7	33.7
×	×	✓	90.5	76.2	94.6	95.8	92.8	84.7	98.6	63.2	18.2	48.4	47.8
✓	✓	×	92.4	<b>86.1</b>	92.4	96.6	<b>98.8</b>	84.8	95.6	64.0	13.4	49.8	<b>40.2</b>
✓	×	✓	91.7	82.9	92.1	94.8	98.3	83.2	99.1	62.1	14.2	48.2	37.6
×	✓	✓	91.1	81.3	89.9	96.7	95.1	84.7	98.7	61.6	15.1	47.3	33.7
✓	✓	✓	<b>92.9</b>	84.0	<b>93.7</b>	96.8	98.4	<b>84.9</b>	<b>99.3</b>	<b>65.9</b>	<b>11.7</b>	<b>47.2</b>	38.0

At the component level, Table 3 shows that DCFA achieves 90.1% mAP50 on NEU-DET, outperforming ELGCA by 1.9 points despite comparable parameter counts, with particularly strong gains on crazing (+16.9 points over ELGCA). On VisDrone, Table 2 shows that DCFA reaches the highest mAP50:95 of 30.1% among all backbone alternatives, suggesting that content-adaptive attention allocation provides more consistent localisation across the ten aerial categories than geometry-driven or token-reduction approaches. As reported in Table 5, DFPN achieves 90.9% mAP50 on NEU-DET, a 3.1-point margin over MSGA, with the Ri category showing the largest per-class gain (+6.7 points), consistent with ANUP preserving the fine-scale edge structure that rolled-in scale defects require. Table 6 shows that FIRC3 reaches 90.5% mAP50, outperforming DGCST by 2.7 points, while also achieving the lowest GFLOPs among all compared fusion modules, as illustrated in Fig. 8.

On VisDrone, DFIR-DETR achieves 51.6% mAP50, a 3.4-point improvement over the RT-DETR baseline and 8.2 points over YOLOv11m, as reported in Table 7. The awning-tricycle category shows the largest per-class gain (+11.7 points

over baseline), a category combining small physical size with an unusual aspect ratio where receptive-field adaptation and high-frequency boundary retention matter most, as illustrated in Fig. 9. Table 8 further compares DFIR-DETR against UAV-specific detectors under the identical 640×640 input protocol. DFIR-DETR surpasses MFP-YOLO and CRL-YOLOv5 by 5.6 and 12.4 percentage points in mAP50 respectively, while achieving the lowest parameter count among all compared Transformer-based methods.

Fig. 10 presents qualitative detection results and GradCAM activation maps on NEU-DET across all six defect categories. Each column corresponds to one category: (a) inclusion, (b) crazing, (c) pitted surface, (d) scratches, (e) rolled-in scale, and (f) patches. For each column, the top row shows the ground truth annotation, the second and third rows show detection results from the RT-DETR baseline and DFIR-DETR respectively, and the bottom two rows show the corresponding GradCAM activation maps.

Across all six categories, DFIR-DETR produces tighter bounding boxes at higher confidence than the baseline. For spatially elongated defects such as scratches (d) and rolled-in

scale (e), the baseline tends to produce loose or fragmented boxes, whereas DFIR-DETR recovers more precise boundary extents. The GradCAM maps tell the same story from the feature side: baseline activations spread broadly across the feature map, whereas DFIR-DETR pulls high-activation regions onto defect boundaries. This contrast is most pronounced in the inclusion (a) and pitted surface (c) categories, where subtle low-contrast textures demand precise high frequency boundary discrimination. The tighter activation footprint is a direct visual signature of the spectral boundary reinforcement that FIRC3 introduces.

## 5. Conclusion

Small object detection in complex, cross-scene environments exposes fundamental tensions in neural network design that cannot be resolved by scaling existing architectures. This work argues that three specific structural properties (uniform attention allocation, amplitude drift during multi-scale fusion, and spectral attenuation through repeated spatial convolution) collectively account for a substantial portion of the performance gap between current detectors and the demands of real-world deployment. DFIR-DETR addresses each through principled architectural interventions: content-adaptive sparse attention in DCFA, norm-preserving feature pyramid construction in DFPN, and frequency-domain iterative refinement in FIRC3. The resulting framework demonstrates that

targeted, theoretically motivated modifications to backbone, neck, and fusion modules can simultaneously improve accuracy, reduce parameters, and maintain real-time throughput without relying on larger training data or heavier model capacity.

Three concrete directions emerge from the limitations of the current design. The frequency-domain computation in FIRC3 stops at the encoder: decoder cross-attention operates entirely in the spatial domain, and there is no mechanism to bias query-key interactions toward boundary-informative spectral components. Introducing a spectral regularisation term into decoder attention could tighten localisation for the sub-16-pixel targets where spatial cues are weakest. The norm-preserving argument behind DFPN currently assumes nearest-neighbour upsampling; the derivation does not carry over to learnable operators such as CARAFE or DySample, whose sampling grids introduce non-uniform amplitude effects that the present normalisation factor does not account for. Finally, DCFA commits to a single sparsity ratio for an entire feature map, which treats a defect cluster and an empty background patch as equally informative. At a modest spatial resolution, Patch-level ratio prediction could redistribute attention budget more precisely without the overhead of full dense computation.

Table 2

Backbone comparison on VisDrone dataset.

Model	mAP50	Ped	Peo	Bic	Car	Van	Tru	Tri	Awn	Bus	Mot	mAP95	Params	GFLOPs	FPS
Strip [33]	48.4	53.8	36.6	23.9	81.4	54.5	57.7	<b>35.7</b>	23.9	68.8	49.9	28.8	14.3	47.7	36.1
MambaOut [34]	46.7	51.1	34.0	22.9	80.2	51.8	53.9	34.4	24.4	65.9	48.2	27.8	15.9	<b>41.9</b>	34.7
GlobalFilter [35]	48.4	53.6	36.7	25.5	81.4	53.4	55.7	34.1	27.4	66.3	50.0	28.7	16.9	46.5	36.9
AP [36]	48.6	53.9	35.8	23.8	81.8	54.6	56.6	34.8	<b>28.1</b>	67.4	49.8	28.9	13.3	47.0	36.9
FDT [37]	47.2	51.7	34.5	24.0	81.5	53.4	53.8	33.6	25.2	65.8	48.1	28.4	15.4	52.5	32.3
DTAB [38]	48.8	55.1	37.9	27.0	<b>82.2</b>	53.6	56.3	34.4	24.7	66.1	51.0	29.3	18.8	57.3	<b>59.9</b>
CAMixer [39]	49.1	53.9	36.8	25.1	81.8	53.5	<b>58.4</b>	35.0	26.8	<b>69.2</b>	50.1	29.4	<b>13.2</b>	43.3	43.2
DCFA (ours)	<b>49.4</b>	<b>55.4</b>	<b>38.1</b>	<b>27.6</b>	<b>82.2</b>	<b>55.1</b>	56.4	35.3	24.4	68.0	<b>51.9</b>	<b>30.1</b>	13.7	51.7	34.2

Table 3

Backbone comparison on NEU-DET dataset.

Model	mAP50	Cr	In	Pa	Ps	Ri	Sr	mAP50:95	Params	GFLOPs	FPS
EfficientViM [40]	87.1	59.3	93.1	96.2	92.8	83.2	98.4	57.5	14.5	47.9	<b>73.1</b>
MambaOut [34]	82.3	64.2	89.4	96.0	93.1	75.5	94.8	54.0	15.9	<b>41.8</b>	59.0
GlobalFilter [35]	88.0	67.2	91.0	96.2	95.5	82.2	95.8	58.5	16.8	46.5	72.3
ELGCA [41]	88.2	62.0	<b>94.6</b>	94.8	92.1	<b>87.3</b>	98.2	60.5	13.9	46.9	38.2
FDT [37]	84.5	57.4	91.4	<b>97.1</b>	92.7	74.0	94.3	55.3	15.4	52.5	32.7
DTAB [38]	84.5	53.5	92.1	95.7	93.1	75.4	96.9	54.3	18.8	57.3	31.8
HDRAB [42]	84.8	49.0	93.6	96.1	90.1	82.4	97.5	56.0	15.6	53.2	37.6
MSN [43]	86.0	53.6	93.2	95.8	94.1	81.2	98.3	59.2	16.6	49.3	32.4
FCA [44]	87.4	63.8	93.4	94.8	91.9	83.9	96.8	58.5	15.4	52.6	31.2
RAB [45]	83.6	48.7	93.1	95.5	90.4	77.8	95.9	54.8	<b>13.3</b>	53.2	34.9
DCFA (ours)	<b>90.1</b>	<b>78.9</b>	91.2	<b>97.0</b>	<b>96.8</b>	84.0	<b>98.6</b>	<b>60.8</b>	13.7	51.7	37.0

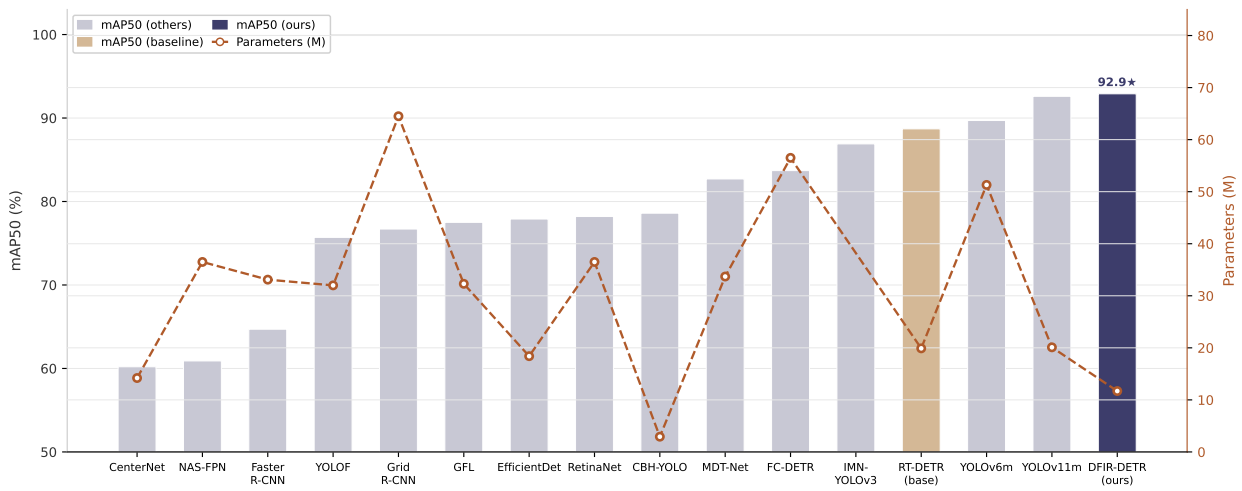


Figure 8: Comparison on NEU-DET.

Table 4

Comprehensive comparison on NEU-DET dataset.

Model	mAP50	Cr	In	Pa	Ps	Ri	Sr	mAP50:95	Params	GFLOPs	FPS
YOLOv6m [46]	89.7	72.0	88.2	96.8	95.2	89.1	96.9	62.1	51.3	158.3	80.4
YOLOv11m [47]	92.6	<b>84.3</b>	90.3	<b>97.0</b>	94.4	<b>92.0</b>	97.1	<b>72.4</b>	20.1	68.0	79.6
YOLOF [48]	75.7	39.7	83.0	90.2	86.1	58.2	97.1	43.7	32.0	52.6	80.5
Faster R-CNN [49]	64.7	30.7	66.9	91.3	67.0	53.9	78.2	29.9	33.1	208.1	18.4
RetinaNet [50]	78.2	50.4	77.8	93.3	89.5	63.9	94.5	43.3	36.5	210.0	68.2
Grid R-CNN [51]	76.7	39.7	82.8	92.5	87.4	60.2	97.5	44.4	64.5	270.2	30.5
GFL [52]	77.5	37.4	84.1	93.9	90.9	62.8	95.9	44.5	32.3	195.2	45.8
NAS-FPN [53]	60.9	29.2	50.0	82.8	79.3	55.6	68.4	26.0	36.5	84.5	–
EfficientDet [19]	77.9	49.8	78.9	93.6	86.8	65.8	92.2	44.6	18.4	55.1	48.9
CenterNet [54]	60.2	22.2	59.3	77.8	77.1	29.7	95.2	27.4	14.2	38.3	48.3
IMN-YOLOv3 [30]	86.9	72.0	86.9	94.8	94.3	80.6	93.2	–	–	–	–
FC-DETR [31]	83.7	67.2	85.8	91.9	88.2	72.5	96.6	–	56.5	143	–
MDT-Net [32]	82.7	50.2	87.4	92.7	86.0	83.0	96.9	55.0	33.7	26.6	18
CBH-YOLO [55]	78.6	53.2	83.0	93.4	82.5	64.6	–	45.8	<b>2.9</b>	<b>7.4</b>	<b>137.1</b>
RT-DETR (base)	88.7	78.4	87.0	96.0	94.6	78.0	98.1	58.2	19.9	57.0	36.9
DFIR-DETR (ours)	<b>92.9</b>	84.0	<b>93.7</b>	96.8	<b>98.4</b>	84.9	<b>99.3</b>	65.9	11.7	47.2	38.0

Table 5

Neck/CCFF module comparison on NEU-DET dataset.

Model	mAP50	Cr	In	Pa	Ps	Ri	Sr	mAP50:95	Params	GFLOPs	FPS
ASF [56]	85.8	56.8	94.7	95.5	93.2	76.6	97.8	57.8	20.2	61.5	39.1
SDI [57]	85.2	54.2	92.7	96.0	93.6	77.2	97.2	57.6	19.9	57.1	35.7
Goldyolo [21]	87.4	62.3	94.6	95.0	94.3	80.6	97.5	58.1	22.3	60.0	32.7
HSFPN [58]	85.2	55.8	92.7	94.9	93.1	78.7	96.2	55.9	<b>18.1</b>	<b>53.3</b>	41.0
CGAFusion [59]	87.0	58.7	93.8	95.6	93.9	83.9	96.4	59.4	20.4	59.2	38.9
PSFM [60]	85.9	55.9	<b>94.9</b>	95.1	93.2	79.3	97.3	58.7	22.4	71.2	26.9
GLSA [61]	85.1	49.3	93.8	95.9	92.7	81.1	97.9	58.2	22.0	63.7	31.1
CTrans [62]	81.6	50.8	87.6	93.3	93.2	71.9	92.7	51.8	29.5	57.4	<b>86.9</b>
MAFFN [63]	83.6	52.6	92.6	95.2	90.4	74.8	96.1	55.5	22.9	56.3	33.8
MSGF [64]	87.8	66.1	93.1	95.3	93.5	82.5	96.6	58.9	22.5	71.1	36.9
FSA [65]	85.0	56.6	94.2	96.2	92.9	73.2	97.1	57.4	22.6	57.0	38.6
MFM [66]	85.8	57.1	93.7	95.8	93.8	77.0	97.3	56.5	19.7	55.7	37.0
DFPN (ours)	<b>90.9</b>	<b>72.1</b>	94.5	<b>97.0</b>	<b>94.4</b>	<b>89.2</b>	<b>98.3</b>	<b>62.6</b>	19.7	56.7	33.7

Table 6

RepC3 module comparison on NEU-DET dataset.

Model	mAP50	Cr	In	Pa	Ps	Ri	Sr	mAP50:95	Params	GFLOPs	FPS
ConvXCC3 [67]	83.5	51.0	93.3	94.9	93.4	70.3	98.3	55.4	19.9	57.0	41.5
DBBC3 [68]	87.2	62.9	91.6	94.6	91.7	85.3	97.3	58.0	19.9	57.0	47.0
DGCST [69]	87.8	65.2	90.5	95.4	<b>95.3</b>	77.6	98.4	56.7	18.5	50.2	42.1
LITC3 [70]	84.3	45.7	94.4	95.6	93.9	78.9	97.5	53.3	19.8	56.0	39.8
FIRC3 (ours)	<b>90.5</b>	<b>76.2</b>	<b>94.6</b>	<b>95.8</b>	92.8	<b>84.7</b>	<b>98.6</b>	<b>63.2</b>	<b>18.2</b>	<b>48.4</b>	<b>47.8</b>

**Table 7**

Comprehensive comparison on VisDrone dataset.

Model	mAP50	Ped	Peo	Bic	Car	Van	Tru	Tri	Awn	Bus	Mot	mAP50:95	Params	GFLOPs	FPS
Faster R-CNN [49]	39.5	39.2	33.0	20.8	74.1	45.8	39.0	30.2	15.1	55.3	42.6	25.6	33.1	208.1	16.5
RetinaNet [50]	32.1	32.1	25.2	13.0	71.4	37.8	35.9	21.5	9.7	43.3	31.9	20.6	36.5	210.0	41.3
FCOS [71]	40.2	45.6	34.6	19.4	78.3	44.2	38.9	28.2	12.9	52.5	47.8	26.1	32.0	203.8	–
Cascade R-CNN [72]	39.1	39.1	31.3	19.3	74.2	46.3	39.2	30.8	13.8	55.1	42.0	26.0	69.3	241.7	13.3
YOLOv5m [73]	33.8	42.6	33.5	11.5	74.3	34.8	30.5	18.4	10.9	40.8	40.9	18.9	19.9	64.2	60.0
YOLOv8m [74]	41.9	44.7	34.7	15.9	80.8	45.9	39.0	31.6	16.2	63.1	47.5	25.1	25.9	78.9	56.3
YOLOv9m [75]	42.0	17.9	37.1	17.8	82.1	50.6	43.6	37.4	20.8	62.7	49.8	27.6	20.0	76.8	62.2
YOLOv10m [76]	41.5	43.6	35.0	15.4	80.5	48.0	40.1	29.9	18.1	58.3	46.6	25.3	15.4	59.1	65.7
YOLOv11m [47]	43.4	48.0	36.2	18.2	82.0	48.6	40.0	32.8	19.3	60.4	49.3	26.5	20.1	68.0	<b>64.5</b>
RT-DETR (base)	48.2	53.2	37.3	<b>25.1</b>	81.3	53.9	56.8	31.8	24.7	67.4	50.1	29.1	19.9	57.0	48.1
DFIR-DETR (ours)	<b>51.6</b>	<b>56.6</b>	<b>39.9</b>	<b>25.1</b>	<b>83.6</b>	<b>55.4</b>	<b>57.8</b>	<b>35.6</b>	<b>36.4</b>	<b>69.6</b>	<b>55.6</b>	<b>31.6</b>	<b>11.7</b>	<b>47.2</b>	40.1

**Table 8**

Comparison with UAV-specific and small-object-oriented methods on VisDrone dataset (640×640 input).

Model	mAP50	mAP50:95	Params	GFLOPs	FPS
MFP-YOLO [77]	46.0	–	<b>1.48</b>	–	28.5
CRL-YOLOv5 [78]	39.2	22.3	–	–	<b>27</b>
AUP-DETR [79]	48.5	29.9	22.7	83.6	–
WDFS-DETR [80]	47.5	–	19.9	53.7	–
TCF-DETR [81]	49.9	29.9	19.8	61.9	–
RT-DETR (base)	48.2	29.1	19.9	57.0	48.1
DFIR-DETR (ours)	<b>51.6</b>	<b>31.6</b>	11.7	<b>47.2</b>	40.1

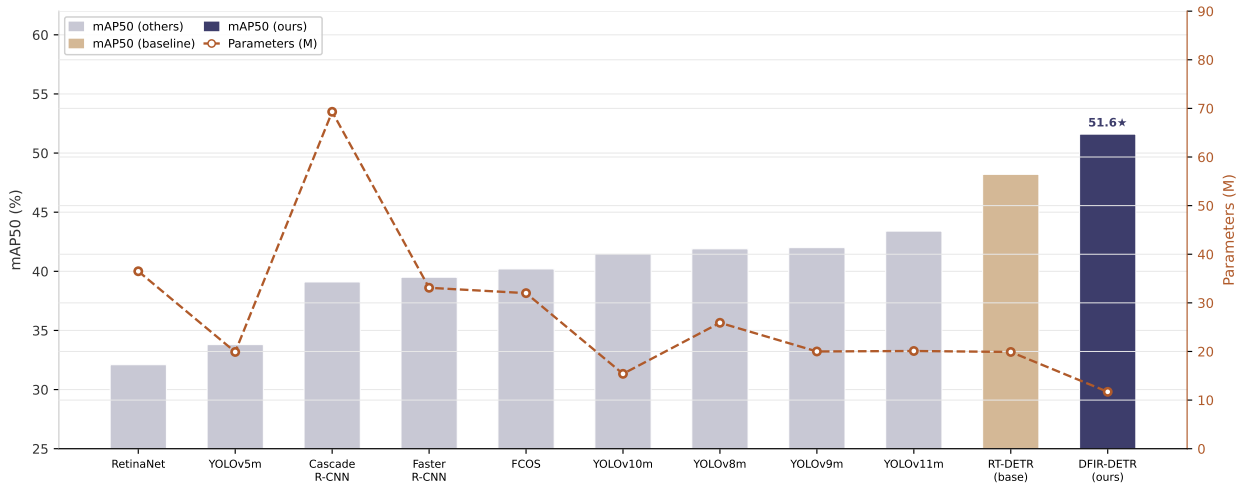


**Figure 9:** Comparison on VisDrone.

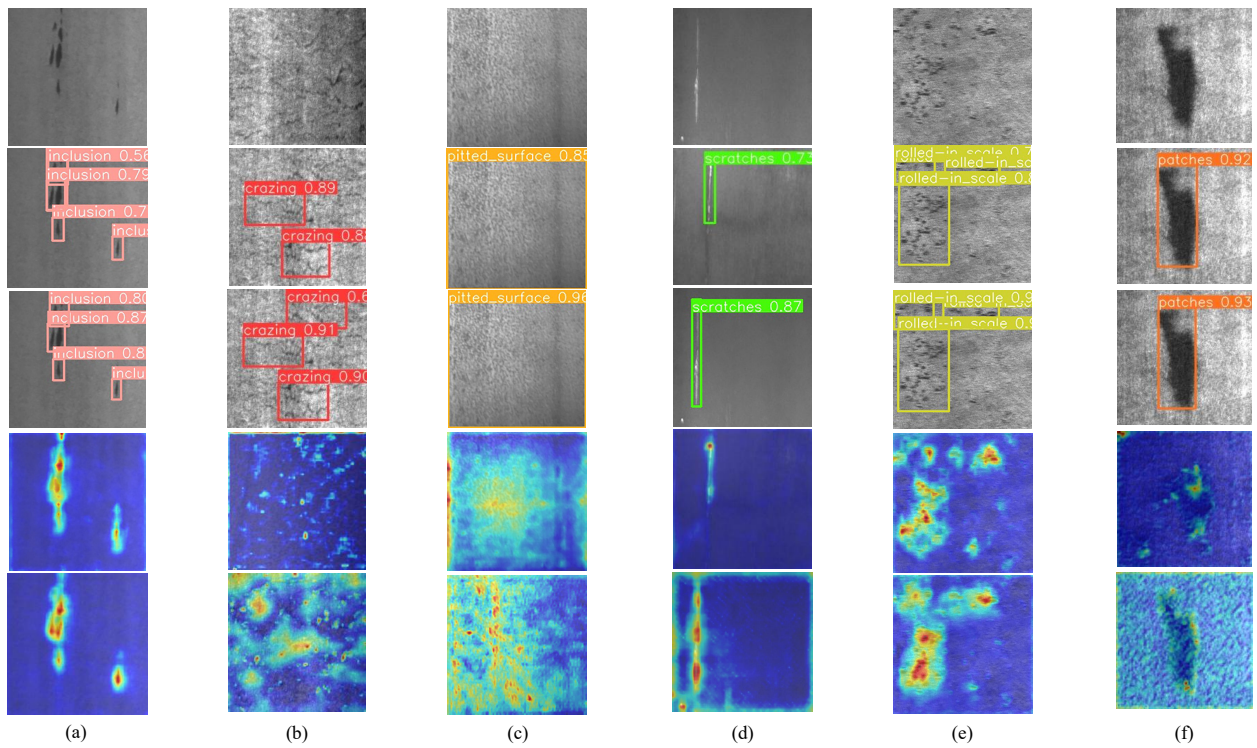


Figure 10: Qualitative visualization comparison on NEU-DET dataset.

## References

- [1] Z. Yuan, J. Gong, B. Guo, C. Wang, N. Liao, J. Song, Q. Wu, Small object detection in uav remote sensing images based on intra-group multi-scale fusion attention and adaptive weighted feature fusion mechanism, *Remote Sensing* 16 (2024) 4265.
- [2] M. Wang, W. Deng, Attention mechanisms in computer vision: A survey, *Computational Visual Media* 10 (2024) 3–25.
- [3] L. Chi, B. Jiang, Y. Mu, Fast fourier convolution, in: *Advances in Neural Information Processing Systems (NeurIPS)*, volume 33, 2020, pp. 4479–4488.
- [4] Y. Zhao, W. Lv, S. Xu, J. Wei, G. Wang, Q. Dang, Y. Liu, J. Chen, Detsr beat yolos on real-time object detection, in: *Proceedings of the IEEE/CVF Conference on Computer Vision and Pattern Recognition (CVPR)*, IEEE, 2024, pp. 16965–16974.
- [5] S. Ren, K. He, R. Girshick, J. Sun, Faster r-cnn: Towards real-time object detection with region proposal networks, *IEEE Transactions on Pattern Analysis and Machine Intelligence* 39 (2017) 1137–1149.
- [6] W. Liu, D. Anguelov, D. Erhan, C. Szegedy, S. Reed, C.-Y. Fu, A. C. Berg, Ssd: Single shot multibox detector, in: *European Conference on Computer Vision*, Springer, 2016, pp. 21–37.
- [7] J. Redmon, S. Divvala, R. Girshick, A. Farhadi, You only look once: Unified, real-time object detection, in: *Proceedings of the IEEE Conference on Computer Vision and Pattern Recognition*, 2016, pp. 779–788.
- [8] J. Redmon, A. Farhadi, Yolov3: An incremental improvement, *arXiv preprint arXiv:1804.02767* (2018).
- [9] N. Carion, F. Massa, G. Synnaeve, N. Usunier, A. Kirillov, S. Zagoruyko, End-to-end object detection with transformers, in: *European Conference on Computer Vision (ECCV)*, 2020, pp. 213–229.
- [10] X. Zhu, W. Su, L. Lu, B. Li, X. Wang, J. Dai, Deformable detr: Deformable transformers for end-to-end object detection, in: *International Conference on Learning Representations (ICLR)*, 2021.
- [11] F. Li, H. Zhang, S. Liu, J. Guo, L. M. Ni, L. Zhang, Dn-detr: Accelerate detr training by introducing query denoising, in: *Proceedings of the IEEE/CVF Conference on Computer Vision and Pattern Recognition (CVPR)*, 2022, pp. 13619–13627.
- [12] H. Zhang, F. Li, S. Liu, L. Zhang, H. Su, J. Zhu, L. M. Ni, H.-Y. Shum, Dino: Detr with improved denoising anchor boxes for end-to-end object detection, in: *International Conference on Learning Representations (ICLR)*, 2023.
- [13] Y. Liu, Y. Tian, Y. Zhao, H. Yu, L. Xie, Y. Wang, Q. Shen, Y. Liu, Vmamba: Visual state space model, *arXiv preprint arXiv:2401.13260* (2024).
- [14] D. Bolya, C.-Y. Fu, X. Dai, P. Zhang, C. Feichtenhofer, J. Hoffman, Token merging: Your ViT but faster, in: *International Conference on Learning Representations (ICLR)*, 2023.
- [15] B. Roh, J. Shin, W. Shin, S. Kim, Sparse DETR: Efficient end-to-end object detection with learnable sparsity, *arXiv preprint arXiv:2111.14330* (2022).
- [16] Z. Yao, J. Ai, B. Li, C. Zhang, Efficient DETR: Improving end-to-end object detector with dense prior, *arXiv preprint arXiv:2104.01318* (2021).
- [17] T.-Y. Lin, P. Dollár, R. Girshick, K. He, B. Hariharan, S. Belongie, Feature pyramid networks for object detection, in: *Proceedings of the IEEE Conference on Computer Vision and Pattern Recognition*, 2017, pp. 936–944.
- [18] S. Liu, L. Qi, H. Qin, J. Shi, J. Jia, Path aggregation network for instance segmentation, in: *Proceedings of the IEEE Conference on Computer Vision and Pattern Recognition*, 2018, pp. 8759–8768.
- [19] M. Tan, R. Pang, Q. V. Le, Efficientdet: Scalable and efficient object detection, in: *Proceedings of the IEEE/CVF Conference on Computer Vision and Pattern Recognition*, 2020, pp. 10781–10790.
- [20] H. Li, J. Li, H. Wei, Z. Liu, Z. Zhan, Q. Ren, Slim-neck by GSCov: A lightweight-design for real-time detector architectures, *Journal of Real-Time Image Processing* 21 (2024) 62.
- [21] C. Wang, W. He, Y. Nie, J. Guo, C. Liu, K. Han, Y. Wang, Gold-yolo: Efficient object detector via gather-and-distribute mechanism, *arXiv preprint arXiv:2309.11331* (2023).
- [22] Y. Tang, K. Han, J. Guo, C. Xu, Y. Li, C. Xu, Y. Wang, An image patch is a wave: Phase-aware vision MLP, in: *Proceedings of the IEEE/CVF Conference on Computer Vision and Pattern Recognition (CVPR)*, 2022, pp. 10935–10944.
- [23] Z. Qin, P. Zhang, F. Wu, X. Li, Fcanet: Frequency channel attention networks, in: *Proceedings of the IEEE/CVF International Conference on Computer Vision (ICCV)*, 2021, pp. 783–792.
- [24] Y. Rao, W. Zhao, Z. Zhu, J. Lu, J. Zhou, Global filter networks for image classification, in: *Advances in Neural Information Processing Systems (NeurIPS)*, volume 34, 2021, pp. 980–993.
- [25] J. Yang, C. Li, X. Dai, J. Gao, Focal modulation networks, in: *Advances in Neural Information Processing Systems (NeurIPS)*, volume 35, 2022, pp. 4203–4217.
- [26] H. Wang, J. Gao, SF-DETR: A scale-frequency detection transformer for drone-view object detection, *Sensors* 25 (2025) 2190.
- [27] J. Chen, N. Liu, H. Sun, Y. Wang, Freq-DETR: Frequency-aware transformer for real-time small object detection in unmanned aerial vehicle imagery, *Expert Systems with Applications* 298 (2025) 129710.
- [28] P. Zhu, L. Wen, D. Du, X. Bian, H. Fan, Q. Hu, H. Ling, Detection and tracking meet drones challenge 44 (2022) 7380–7399.
- [29] K. Song, Y. Yan, A noise robust method based on completed local binary patterns for hot-rolled steel strip surface defects, *Applied Surface Science* 285 (2013) 858–864.
- [30] X. Chen, J. Lv, Y. Fang, S. Du, Online detection of surface defects based on improved YOLOV3, *Sensors* 22 (2022) 817.
- [31] F. Li, et al., FC-DETR: High-precision end-to-end surface defect detector based on foreground supervision and cascade refined hybrid matching, *Expert Systems with Applications* 266 (2025) 126142.
- [32] H. Wang, F. Zhang, R. Yi, Multi-scale deformable transformer with iterative query refinement for hot-rolled steel surface defect detection, *Sensors* 25 (2025) 6890.
- [33] Z. Guo, L. Leng, Y. Wu, C. Li, Y. Wang, Q. Zhang, Strip: Spatial transformer for efficient image processing, *Pattern Recognition* 135 (2023) 109139.
- [34] W. Yu, X. Wang, Mambaout: Do we really need mamba for vision?, *arXiv preprint arXiv:2405.07992* (2024).
- [35] Y. Rao, W. Zhao, Y. Tang, J. Zhou, S.-N. Lim, J. Lu, Global filter networks for image classification, in: *Advances in Neural Information Processing Systems*, volume 35, 2022, pp. 980–993.
- [36] J. Dai, H. Qi, Y. Xiong, Y. Li, G. Zhang, H. Hu, Y. Wei, Deformable convolutional networks, in: *Proceedings of the IEEE International Conference on Computer Vision*, 2017, pp. 764–773.
- [37] Y. Mao, H. Zhou, J. Xia, K. Zhang, Fdt: Fast and effective dynamic token for vision transformer, in: *Proceedings of the IEEE/CVF International Conference on Computer Vision*, 2023, pp. 7598–7607.
- [38] Z. Liu, Y. Han, Q. Zhang, K. Li, Dtab: Dual-token attention block for efficient vision transformers, *IEEE Transactions on Circuits and Systems for Video Technology* 33 (2023) 4163–4177.
- [39] Z. Tu, H. Talebi, H. Zhang, F. Yang, P. Milanfar, A. Bovik, Y. Li, Camixer: Convolution and attention mixing for efficient image processing, in: *Proceedings of the IEEE/CVF International Conference on Computer Vision*, 2023, pp. 2589–2599.
- [40] J. Zhu, J. Li, J. Chen, Q. Chen, Efficientvim: Efficient vision mamba with bidirectional state space models for semantic segmentation, *arXiv preprint arXiv:2402.02509* (2024).
- [41] L. Song, M. Xia, L. Weng, H. Lin, M. Qian, B. Chen, Elgca: Efficient local-global context aggregation for remote sensing change detection, *IEEE Geoscience and Remote Sensing Letters* 21 (2024) 1–5.
- [42] X. Wang, D. Liu, Y. Song, D. Liang, Hdrab: High-dynamic range attention block for efficient image super-resolution, *Pattern Recognition* 139 (2023) 109451.
- [43] Z. Huang, J. Wang, X. Fu, T. Yu, Y. Guo, R. Wang, Msn: Multi-scale network for object detection, in: *Proceedings of the IEEE/CVF Conference on Computer Vision and Pattern Recognition*, 2023, pp. 3368–3378.
- [44] Z. Qin, P. Zhang, F. Wu, X. Li, Fcanet: Frequency channel attention networks, *arXiv preprint arXiv:2012.11879* (2020).

- [45] W. Yang, Y. Yuan, W. Guo, W. Ren, J. Zhang, X. He, S. Kwong, S. Wang, Rab: Residual attention block for efficient image super-resolution, in: Proceedings of the IEEE/CVF International Conference on Computer Vision Workshops, 2021, pp. 1477–1486.
- [46] C. Li, L. Li, H. Jiang, K. Weng, Y. Geng, L. Li, Z. Ke, Q. Li, M. Cheng, W. Nie, et al., Yolov6 v3.0: A full-scale reloading, arXiv preprint arXiv:2301.05586 (2023).
- [47] Ultralytics, Yolov11: An improved real-time object detection model, <https://docs.ultralytics.com>, 2024.
- [48] Q. Chen, Y. Wang, T. Yang, X. Zhang, J. Cheng, J. Sun, You only look one-level feature (2021) 13039–13048.
- [49] S. Ren, K. He, R. Girshick, J. Sun, Faster r-cnn: Towards real-time object detection with region proposal networks, IEEE Transactions on Pattern Analysis and Machine Intelligence 39 (2017) 1137–1149.
- [50] T.-Y. Lin, P. Goyal, R. Girshick, K. He, P. Dollár, Focal loss for dense object detection, in: Proceedings of the IEEE International Conference on Computer Vision, 2017, pp. 2980–2988.
- [51] X. Lu, B. Li, Y. Yue, Q. Li, J. Yan, Grid r-cnn, in: Proceedings of the IEEE/CVF Conference on Computer Vision and Pattern Recognition, 2019, pp. 7363–7372.
- [52] X. Li, W. Wang, L. Wu, S. Chen, X. Hu, J. Li, J. Tang, J. Yang, Generalized focal loss: Learning qualified and distributed bounding boxes for dense object detection, in: Advances in Neural Information Processing Systems, volume 33, 2020, pp. 21002–21012.
- [53] G. Ghiasi, T.-Y. Lin, R. Pang, Q. V. Le, Nas-fpn: Learning scalable feature pyramid architecture for object detection, in: Proceedings of the IEEE/CVF Conference on Computer Vision and Pattern Recognition, 2019, pp. 7036–7045.
- [54] X. Zhou, D. Wang, P. Krähenbühl, Objects as points, 2019.
- [55] B. Gao, J. Tong, R. Fu, Z. Zhang, Y. Yuan, CBH-YOLO: A steel surface defect detection algorithm based on cross-stage Mamba enhancement and hierarchical semantic graph fusion, Neurocomputing 656 (2025) 131467.
- [56] C. Yang, Z. Huang, N. Wang, Asf: Adaptive spatial fusion for efficient multi-scale feature learning, arXiv preprint arXiv:2202.03149 (2022).
- [57] H. Zhao, J. Shi, X. Qi, X. Wang, J. Jia, Sdi: Spatial detail injection network for multi-scale semantic segmentation, Pattern Recognition 138 (2023) 109367.
- [58] Y. Li, Q. Hou, Z. Zheng, M.-M. Cheng, J. Yang, X. Li, Hsfpn: Hierarchical semantic fusion pyramid network for multi-scale object detection, IEEE Transactions on Image Processing 32 (2023) 2918–2931.
- [59] H. Guo, J. Yang, B. Yang, G. Xu, Cgafusion: Context-guided adaptive fusion network for rgb-t semantic segmentation, in: Proceedings of the IEEE/CVF Conference on Computer Vision and Pattern Recognition Workshops, 2023, pp. 4156–4165.
- [60] P. Sun, R. Zhang, Y. Jiang, T. Kong, C. Xu, W. Zhan, M. Tomizuka, L. Yuan, P. Wang, P. Luo, Psfm: Progressive semantic feature module for object detection, arXiv preprint arXiv:2302.02923 (2023).
- [61] Y. Zhang, K. Li, K. Li, L. Wang, B. Zhong, Y. Fu, Glsa: Global-local self-attention for multi-scale feature learning, IEEE Transactions on Pattern Analysis and Machine Intelligence 45 (2023) 8784–8800.
- [62] X. Yan, H. Tang, S. Sun, H. Ma, D. Kong, X. Xie, Ctrans: Cross-transformer network for multi-scale feature fusion, in: Proceedings of the IEEE/CVF International Conference on Computer Vision, 2023, pp. 3868–3877.
- [63] W. Liu, Z. Wang, X. Liu, N. Zeng, Y. Liu, F. E. Alsaadi, Maffn: Multi-scale attention feature fusion network for semantic segmentation, Neurocomputing 520 (2023) 29–40.
- [64] J. Wang, K. Chen, J. Yang, C. C. Loy, D. Lin, Msga: Multi-scale grouped attention mechanism for object detection, Pattern Recognition 140 (2023) 109545.
- [65] X. Li, A. You, Z. Zhu, H. Zhao, M. Yang, K. Yang, Y. Tong, Fsa: Feature separation and aggregation network for semantic segmentation, Neurocomputing 523 (2023) 103–114.
- [66] J. Hu, L. Shen, G. Sun, Mfm: Multi-frequency multiscale feature fusion for object detection, in: Proceedings of the AAAI Conference on Artificial Intelligence, volume 37, 2023, pp. 860–868.
- [67] X. Ding, X. Zhang, N. Ma, J. Han, G. Ding, J. Sun, Diverse branch block: Building a convolution as an inception-like unit, in: Proceedings of the IEEE/CVF Conference on Computer Vision and Pattern Recognition, 2021, pp. 10886–10895.
- [68] K. Han, Y. Wang, Q. Tian, J. Guo, C. Xu, C. Xu, Dbbc3: Dynamic branching bottleneck for efficient neural networks, IEEE Transactions on Neural Networks and Learning Systems 34 (2023) 4456–4468.
- [69] X. Chen, H. Wang, Y. Hong, J. Guo, X. Wang, Q. Zhang, Dgcs: Dynamic group convolution shuffle transformer for efficient vision backbone, Pattern Recognition Letters 168 (2023) 36–43.
- [70] Z. Liu, Y. Lin, Y. Cao, H. Hu, Y. Wei, Z. Zhang, S. Lin, B. Guo, Litv2: Efficient self-attention for vision transformers with learnable interaction tokens, in: Proceedings of the IEEE/CVF Conference on Computer Vision and Pattern Recognition, 2023, pp. 11043–11053.
- [71] Z. Tian, C. Shen, H. Chen, T. He, Fcos: Fully convolutional one-stage object detection, in: Proceedings of the IEEE/CVF International Conference on Computer Vision, 2019, pp. 9627–9636.
- [72] Z. Cai, N. Vasconcelos, Cascade r-cnn: Delving into high quality object detection, in: Proceedings of the IEEE Conference on Computer Vision and Pattern Recognition, 2018, pp. 6154–6162.
- [73] Ultralytics, Yolov5: A state-of-the-art real-time object detection system, <https://github.com/ultralytics/yolov5>, 2021.
- [74] G. Jocher, A. Chaurasia, J. Qiu, Ultralytics YOLOv8, 2023. URL: <https://github.com/ultralytics/ultralytics>.
- [75] C. Y. Wang, H. Y. Liao, Yolov9: Learning what you want to learn using programmable gradient information, arXiv preprint arXiv:2402.13616 (2024).
- [76] A. Wang, H. Chen, L. Liu, K. Chen, Z. Lin, J. Han, G. Ding, Yolov10: Real-time end-to-end object detection, arXiv preprint arXiv:2405.14458 (2024).
- [77] M. Li, et al., Lightweight object detection algorithm for UAV aerial imagery, ISPRS International Journal of Geo-Information 12 (2023) 261.
- [78] M. Zhang, et al., Improved small object detection algorithm CRL-YOLOv5, Sensors 24 (2024).
- [79] J. Xu, X. Liu, X. Li, Y. Hu, AUP-DETR: A foundational UAV object detection framework for enabling the low-altitude economy, Drones 9 (2025) 822.
- [80] J. Liu, Y. Xie, WDFS-DETR: A transformer-based framework with multi-scale attention for small object detection in UAV engineering tasks, Results in Engineering 27 (2025) 105930.
- [81] H. Lei, Z. Wu, L. Shang, H. Zhao, W. Yang, TCF-DETR: Multi-scale token-channel fusion transformer for enhanced small object detection, Multimedia Systems 31 (2025) 292.